REFERENCES AND NOTES

1. J. R. Cochran, *Am. Assoc. Pet. Geol. Bull.* **67**, 41 (1983).
2. ______, J.-M. Gaulier, X. LePichon, *Tectonics* **10**, 1018 (1992).
3. V. Courtillot, *ibid.* **1**, 239 (1982).
4. E. Bonatti, *Nature* **316**, 33 (1985).
5. B. P. Kohn and M. Eyal, *Earth Planet. Sci. Lett.* **52**, 129 (1981).
6. G. I. Omar, B. P. Kohn, T. M. Lutz, H. Faul, *ibid.* **83**, 94 (1987).
7. G. I. Omar, M. S. Steckler, W. R. Buck, B. P. Kohn, *ibid.* **94**, 316 (1989).
8. R. G. Bohannon, C. W. Naeser, D. L. Schmidt, R. A. Zimmermann, *J. Geophys. Res.* **94**, 1683 (1989).
9. J. Braun and C. Beaumont, *Geology* **17**, 760 (1989).
10. J. K. Weissel and G. D. Karner, *J. Geophys. Res.* **94**, 13919 (1989).
11. P. van der Beek, S. Cloetingh, P. Andriessen, *Earth Planet. Sci. Lett.* **121**, 417 (1994).
12. Preparation of samples for FT analysis, irradiation, counting, track length measurements, calibration techniques, and error calculations are described in (*7*).
13. Z. Garfunkel, *Tectonophysics* **150**, 33 (1988).
14. M. S. Steckler, F. Berthelot, N. Lyberis, X. LePichon, *ibid.* **153**, 249 (1988).
15. G. R. Willgoose, R. L. Bras, I. Rodriguez-Iturbe, *Water Resour. Res.* **27**, 1685 (1991).
16. M. S. Steckler and G. I. Omar, *J. Geophys. Res.* **99**, 12159 (1994).
17. C. Montenat *et al.*, *Tectonophysics* **153**, 161 (1988).
18. J. S. Pallister, *Geol. Soc. Am. Bull.* **99**, 400 (1987).
19. D. L. Schmidt, D. G. Hadley, G. F. Brown, *U.S. Geol. Surv. Open-File Rep. 83-641* (1983).
20. R. G. Bohannon, *Geology* **14**, 510 (1986).
21. H. J. Bayer, H. Hötzl, A. R. Jado, B. Roscher, W. Voggenreiter, *Tectonophysics* **153**, 137 (1988).
22. R. G. Coleman, R. T. Gregory, G. F. Brown, *U.S. Geol. Surv. Open-File Rep. 83-788* (1983).
23. A. Y. Izzeldin, thesis, University of Louis Pasteur, Strasbourg (1982).
24. V. E. Camp and M. J. Roobol, *J. Geophys. Res.* **97**, 15255 (1992).
25. I. Davison *et al.*, *Geol. Soc. Am. Bull.* **106**, 1474 (1994).
26. R. G. Bohannon and S. Eittreim, *Tectonophysics* **198**, 129 (1991).
27. W. Bosworth, *J. Geol. Soc. London Spec. Pub.* **80**, 75 (1995).
28. M. Richardson and M. A. Arthur, *Mar. Petrol. Geol.* **5**, 247 (1989).
29. R. G. Coleman and A. McGuire, *Tectonophysics* **150**, 77 (1988).
30. R. Carella and N. Scarpa, *Proc. Fourth Arab Petrol. Congr.* (1962).
31. D. C. Almond, *Tectonophysics* **131**, 301 (1986).
32. R. G. Coleman, S. DeBari, Z. Peterman, *ibid.* **204**, 27 (1992).
33. A. M. C. Sengör and K. Burke, *Geophys. Res. Lett.* **5**, 419 (1978).
34. H. A. Roeser, *Geol. Jahrb.* **D13**, 131 (1975).
35. The data table and sample coordinates for the FT analysis are available on request from G.I.O.

This work was supported by NSF grants EAR 89-17154 (G.I.O.) and EAR 89-16976 (M.S.S.). A special debt of gratitude is owed to the University of Pennsylvania Research Foundation for providing funds to modernize the fission-track laboratory. We thank R. Bohannon and C. Naeser for providing the apatite fractions from southwestern Saudi Arabia. This is Lamont-Doherty Earth Observatory publication number 5404.

10 July 1995; accepted 21 September 1995

Relation of the 1992 Landers, California, Earthquake Sequence to Seismic Scattering

Justin Revenaugh

Measurements of crustal scattering for the area surrounding the 1992 Landers earthquake sequence obtained from regional array recordings of teleseismic events for the 10-year period before the sequence showed that the slip distribution on faults could be deducible from the preshock elastic structure. Scattering intensity correlated strongly with the distribution of aftershocks and slip of the moment magnitude (M_w) 7.3 Landers main shock, M_w 6.1 Joshua Tree, and M_w 6.2 Big Bear events, which implies that aftershocks and slip are structurally controlled and broadly predictable. Scattering within the fault zones was directional and consistent with variable along-strike alignment of stress-induced cracks.

There is abundant evidence that fault bends and jumps play a major role in producing along-fault slip variability and frequently serve as the nucleation point or termination point of major earthquakes (*1*). Evidence about the importance of fault-zone elastic heterogeneity is also accumulating. Recent high-resolution seismic tomography experiments have revealed that the distributions of aftershocks and main shock slip are associated with high-velocity patches within the fault zone, thus implicating fault zone strength as a primary control on earthquake slip (*2*). However, such surveys usually require rich aftershock sequences as the source array necessary for adequate spatial resolution, and thus long, quiescent segments cannot be sampled. Because it is often these segments that are of greatest societal concern, the need for an alternative mode of imaging is clear.

To this end, I have developed a scheme for estimating the short scale length variability in crustal scattering strength on the basis of regional array recordings of teleseismic events (*3*). Because it does not rely on regional or local seismicity, the method, referred to as Kirchhoff coda migration (KCM), is applicable to locked fault segments. Here I report on a ground-truthing experiment that correlated scattering-derived estimates of fault zone heterogeneity to aftershock and slip distributions of the M_w 6.1 Joshua Tree, M_w 7.3 Landers, and M_w 6.2 Big Bear earthquakes in southern California, a foreshock–main shock–aftershock sequence in April through June 1992. The Landers sequence is the most extensively recorded sequence to have occurred in southern California, and its main shock slip is well modeled (*4*).

As a function of velocity and density variability, scattering potential is a good indicator of short scale length crustal heterogeneity (*5*) (Fig. 1A). However, the extent to which it is an indicator of fault zone heterogeneity is not immediately clear from Fig. 1B, which reveals little overall correlation of scattering potential with mapped fault traces, as both highs and lows occur along fault zones (*6*). Nonetheless, several lines of evidence point to a strong component of fault-induced scattering: (i) The correlation length scale of scattering potential (~8 km) is equal to the length scales of seismicity and active fault density (*7*); by comparison, the length scale of topography is greater by a factor of ~4 (~30 km), which indicates that scattering is sensitive to heterogeneity with dimensions characteristic of faulting, not topography. (ii) Contours of aftershock density are deflected where they meet high scattering gradients and visibly neck at crossings (Fig. 1C), which suggests that transitions between high and low scattering delimit fault segments. (iii) The collinear aftershock zones of the Joshua Tree and Landers events follow a series of scattering highs, Big Bear aftershocks are aligned along a pronounced scattering low, and seismicity as a whole clusters near the scattering extremes. (iv) Short scale length variations in scattering potential along the Joshua Tree, Landers, and Big Bear fault zones are associated with aftershock density (Fig. 2). For example, the correlation coefficient measured within a 12.5-km-wide band tracing the Landers fault zone exceeds 0.8 (*8*). Viewed in this way, the scattering potential and gradient clearly are responding to heterogeneity that directly influences aftershock distribution, but the functional form of the relation is complicated by the reversed sense of correlation for the Big Bear sequence.

An assumption used in KCM is that scattering is isotropic; however, because *P*-wave to *S*-wave scattering is not isotropic (*9*), we must be careful to distinguish estimated scattering potential from local scatterer strength, because the latter may be distinctly anisotropic. The northwest alignment of scattering highs and the northeast alignment of lows in Fig. 1B—dominated by the Joshua Tree–Landers and Big Bear aftershock zones, respectively—suggest directional scattering. To test this suggestion, I subdivided the

Crustal Imaging Laboratory, Earth Sciences Department, University of California, Santa Cruz, CA 95064, USA.

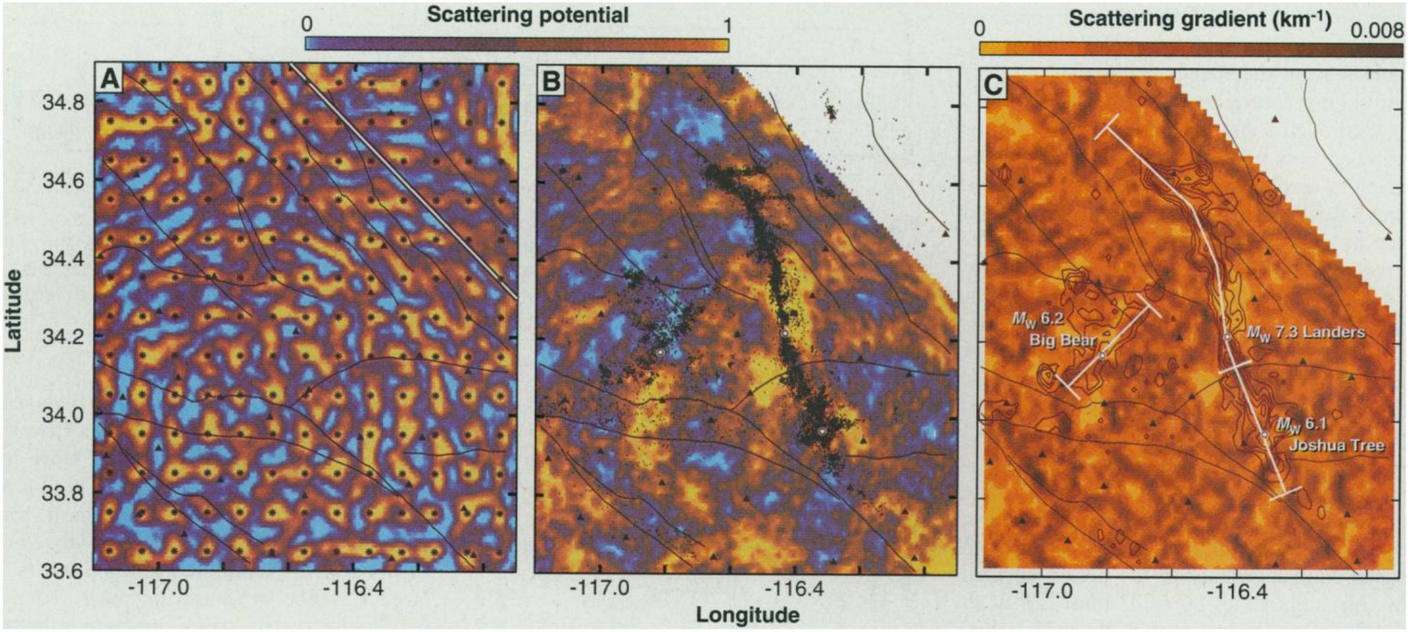

Fig. 1. (**A**) Depth slice at 10 km of the *P to* S_g (teleseismic *P* scattered into up-going *S*) KCM volume for a synthetic data set that exactly replicates the actual experiment in terms of data volume and geometry. A 0.1° by 0.1° grid of point scatterers at a depth of 10 km (indicated by asterisks) was used to create the data set that includes both *P* and *S* scattered waves, realistic travel-time and amplitude variability, strong attenuation, and high-amplitude random noise. Seismograms were low-pass–filtered below 1 Hz; further details of data processing are discussed in (*3*). Shown is a contour plot of scattering potential—the significance of scattering relative to background levels inferred from bootstrap iteration on randomized data sets—resolved on a 0.01° by 0.01° grid. A scattering potential near unity implies large amounts of scattered energy, whereas zero implies very small amounts. Black triangles mark stations of the Southern California Seismic Network recording the 81 teleseismic events used in the KCM (additional stations outside the plot bounds were used). With the exception of the northeast corner of the study area, horizontal resolution of scatterer location and strength is quite good, the result of KCM's sensitivity to the travel time of scattered energy as opposed to the travel-time residuals sensed in tomography. Vertical resolution is poorer, such that the image is a vertical average of scattering strength between 5 and 15 km. (**B**) Depth slice at 10 km of the *P* to S_g scattering volume for the Landers area of southern California obtained from the use of a regional, one-dimensional velocity model [the "Landers" model of Hauksson *et al.* (*12*) scaled for shear waves]. Resolution in the northeast corner is low, and no result was sought there [see (A)]. Black dots are epicenters of local magnitude (M_L) ≥ 2 aftershock seismicity through 1994. (**C**) Magnitude of the horizontal gradient of scattering potential at a depth of 10 km. Aftershock density is represented by solid-line contours. Fault zones of the Joshua Tree, Landers, and Big Bear earthquakes used to calculate correlations between scattering and aftershock statistics are shown in white.

event catalog into two sets of nearly equal size: one composed of events in Japan and South America (JSA), the other of events in Tonga-Fiji and the New Hebrides (TF). Great circle paths of JSA events are subparallel across southern California, trending at roughly N53°W as compared with N57°E for events in the TF set. Separate KCM of these two data sets reveals significant variation of scattering along parts of the Joshua Tree–Landers fault zone, with some highs paired to lows between images.

The Big Bear scattering potential is more constant, although it is slightly stronger in the image derived from JSA events. I attribute this behavior to anisotropic scattering. In particular, the pronounced low along the Big Bear aftershock zone appears to be the result of highly directional scattering that is not well excited by either source region set. If fault-aligned cracks are the dominant sources of scattering within the fault zone, scattering of *P* waves incident parallel and perpendicular to the fault strike will be inefficient (*10*). Because the Big Bear zone trends at roughly 80° to JSA great circle paths and at roughly 10° to TF paths, this appears to be a plausible explanation for the pronounced scattering low, provided that off-fault scattering is either less directional or more favorably aligned and thus defines a background level above a poorly illuminated Big Bear fault zone. By comparison, fault segments of the Landers and Joshua Tree events strike a minimum of 12° from one of the two source areas, with an average strike separation of near 30° (*11*). Only the northernmost (Camp Rock) segment of the Landers fault zone has angles as low as those of Big Bear relative to both source region sets; the

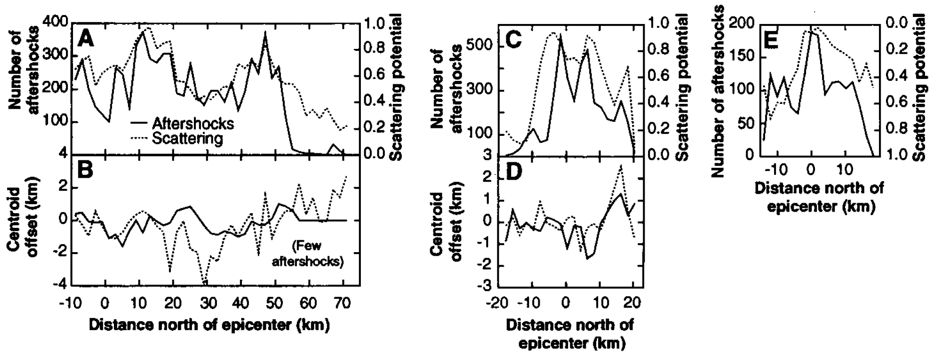

Fig. 2. (**A**) Comparison of along-fault variation in mean scattering potential and number of aftershocks within a 12.5-km-wide box centered on the Landers fault zone. Distance is measured along the fault zone shown in Fig. 1C, and statistics have been computed for nonoverlapping 2-km bins. Only M_L ≥ 2 events are used; other cutoff thresholds produced similar results. (**B**) Comparison of aftershock centroid offset [mean fault-normal displacement from the center line of the assumed fault zone (Fig. 1C)] versus the scattering centroid offset (mean fault-normal distance weighted by scattering potential). The strong correlation implies that aftershocks track scattering highs. (**C** and **D**) Comparisons similar to (A) and (B) for the Joshua Tree fault zone. (**E**) Comparison for the Big Bear fault zone. Note the reversed scale for scattering potential. The Big Bear event occurred in an area of low apparent scattering that I attribute to poor illumination of highly directional scattering, not intrinsically weak scattering.

scattering highs east of that segment appear to be a result of the east-west–striking conjugate faults seen in the aftershock distribution (*12*) and do not contradict this hypothesis.

Although some form of scattering anisotropy appears necessary, fault-aligned microfractures and cracks are not the only possible cause. Rock fabric may be important and need not be fault-aligned if it records an earlier stress state (*13*), but rock fabric is typically subordinate to crack-induced anisotropy at the upper crustal depths of interest (*14*). Because of the approximate fourfold symmetry of scattering with respect to crack orientation, fault-normal cracks are an admissible alternative. Extensive-dilatancy anisotropy (EDA) refers to the anisotropy produced by the alignment of fluid-filled microcracks parallel to the direction of greatest principal confining stress, σ_1 (*15*). The orientation of σ_1 inferred from background seismicity in the period covered by this study varies by ~25° from N3°W in the Big Bear region to N20°E near Joshua Tree and Landers (*16*). This variation is approximately the difference in illumination angles inferred above from fault strikes; thus, EDA may be a potential explanation for the apparent contrast in scattering between Landers and Big Bear. It is difficult to explain why scattering at Big Bear falls below the local background level, however, because the fault does not strongly influence the local orientation of σ_1 (*16*).

Given this constraint and near-fault observation of fault-parallel alignment of fast S-wave polarization (*17, 18*), I favor fault-aligned cracks as the dominant source of scattering within the fault zone. I interpret the scattering low along the Big Bear fault as the result of limited illumination aperture to reconcile the apparent negative correlation of scattering strength and aftershock density with the strong positive correlation observed for Landers and Joshua Tree. In summary, scattering potential is correlated to aftershock density, and the sense of correlation is contingent on fault-zone illumination but consistent with greater crack density and degree of fault alignment in areas of high aftershock density.

Both asperity and barrier models of fault rupture predict complementary distributions of main shock slip and aftershocks. In the asperity model, aftershocks populate weak zones surrounding the strong asperity, whereas in the barrier model, aftershocks represent the delayed failure of strong barriers to main shock rupture. Interpreting the correlation of aftershock density and scattering potential in terms of these models leads to two different conclusions: strong scattering in weak zones for the asperity model versus strong scattering in strong zones for the barrier model. Scattering potential that scales with crack density favors the barrier model, because slip loading of

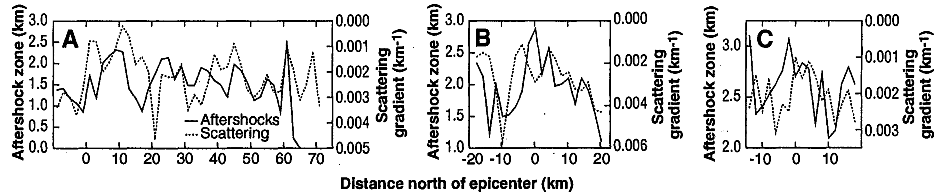

Fig. 3. Comparison of scattering potential gradient to aftershock density and aftershock zone width (measured as the standard deviation of aftershock fault-normal displacement from the center line of the fault zone). (**A**) Landers fault zone; (**B**) Joshua Tree fault zone; (**C**) Big Bear fault zone. Aftershocks are fewer and more tightly clustered in regions of high gradient (see also Fig. 1C), which suggests a narrowed fault zone with greater main shock stress release in these areas.

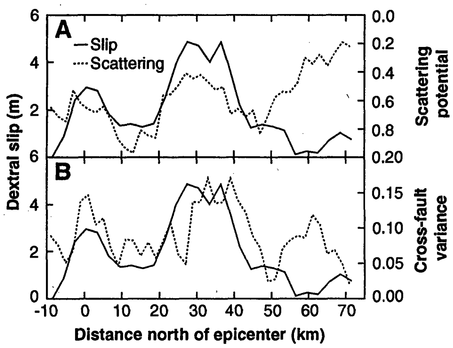

Fig. 4. Comparison of (**A**) scattering potential and (**B**) cross-fault scattering variance (*22*) to dextral slip at a depth of 10 km (*21*). Cross-fault scattering variance is greatest for narrow fault segments. The positive correlation of slip and scattering variance implies high slip along narrow fault segments. This finding and low slip within strong scattering segments favor a barrier model of main shock rupture, with high-scattering-potential segments acting as barriers to slip and areas of broadly distributed strain separating weak fault spans.

barriers results in increased stress and, through repeated rupture, in a greater density of stress-induced cracks. The concentration of stress in barriers affects a broad zone and results in a lower scattering gradient, as evidenced by its negative correlation with aftershock density and aftershock zone width (Fig. 3). The alternative is to associate asperities with low scattering strengths (that is, low crack densities) before rupture, which conflicts with their interpretation as high-stress patches before rupture (*19*).

Two related but unresolved issues are the size distribution of cracks and possible temporal variation of crack-induced scattering. It is conceivable that stress accumulation before rupture influences crack aperture and therefore the strength of scattering, such that KCM images obtained from data recorded further in advance of, or after, the Landers sequence may differ from that presented here. Regional increases in field-scale (≥1 m) crack density are conjectured to cause 2- to 20-year variations in coda duration correlated with earthquake productivity (*20*).

For the Landers event, slip at depth (*21*) decreased rapidly upon entry into high scattering areas [rupture propagated northward, north of the epicenter (Fig. 4)]. More important, slip is correlated to cross-fault scattering variance, a measure of fault zone width (*22*). A narrow fault zone (that is, a thin band of strong scattering) results in large variance in scattering measured perpendicular to the strike, whereas a broadened zone produces uniform scattering and little or no cross-fault variance. The association of greatest slip with a narrowed fault zone also favors the barrier model because high-slip, high-stress asperities would be expected to disrupt a greater volume of crust. The apparent structural control on slip argues against variable loading as the cause of nonuniform slip distribution. Conversely, it argues for simultaneous or penecontemporaneous prior rupture of the Johnson Valley, Landers, Homestead Valley, Emerson, and Camp Rock faults comprising the Landers rupture zone, because earlier segmented ruptures should have produced variations in 1992 slip attributable to available energy and not predictable from the scattering potential. This hypothesis is consistent with paleoseismological estimates of the date of last rupture of these component faults (*23*).

The vertical resolution achievable with KCM is about 10 km, such that the scattering estimates (assuming scatterers at 10 km) are upper crustal averages appropriate for depths of ~5 to 15 km. KCM images obtained when scatterers are assumed to be at depths of 2 and 20 km, although substantially similar in form, yield consistently lower correlation coefficients with aftershock statistics. This remains the case for a number of aftershock magnitude cutoffs and depth range restrictions. Because depths of 5 to 15 km coincide with the seismogenic zone, optimal correlation at these depths is not surprising. However, the inference of crack-induced anisotropy at these depths, although consistent with observations of fluid-filled inclusions throughout the upper ~20 km of crust (*24*) and some seismic studies (*17, 20, 25*), extends the base of crack anisotropy deeper than many seismic estimates (*18*). The inferred deep anisotropy may be unique to these fault zones but more likely reflects the differing sensitivities and modes of fault zone sampling of scattered-wave migration and polarization–travel-time analysis. Extensive fault-parallel cracking at seismogenic depths could provide a high-permeability channel for along-fault fluid flow (*15*, *26*).

The observed correlations of scattering potential, aftershock distribution, and coseismic slip imply that structure places a strong control on rupture over length scales much greater than event slip and thus at scales that should evolve slowly with respect to the earthquake cycle. This observation is favorable to the notion of repeatable events, but only inasmuch as the pattern of slip variability along individual fault segments is concerned. Scattering potential provides no clear indication of the initiation or termination of rupture; that is, there is no characteristic property of scattering that delimits rupture, only a correspondence between scattering and rupture where rupture has occurred. Lastly, the correlation of aftershock density with structural heterogeneity measured before rupture suggests that main shock–induced changes affecting aftershock production are structurally related or of second-order importance. Insofar as they affect scattering, KCM images made from recordings since the Landers sequence should reveal them.

REFERENCES AND NOTES

1. R. H. Sibson, in *Earthquake Source Mechanics*, S. Das, J. Boatwright, C. Scholz, Eds. (*Geophysical Monograph* **37**, American Geophysical Union, Washington, DC, 1986), pp. 157–168; G. King and J. Nábělek, *Science* **228**, 984 (1985).
2. A. J. Michael and D. Eberhart-Phillips, *Science* **253**, 651 (1991); C. Nicholson and J. M. Lees, *Geophys. Res. Lett.* **19**, 1 (1992); J. M. Lees and C. Nicholson, *Geology* **21**, 387 (1993); W. Foxall, A. Michelini, T. V. McEvilly, *J. Geophys. Res.* **98**, 17691 (1993); D. Zhao and H. Kanamori, *Geophys. Res. Lett.* **20**, 1083 (1993); *ibid.* **22**, 763 (1995).
3. J. Revenaugh, *Geophys. Res. Lett.* **22**, 543 (1995); *Science* **268**, 1888 (1995).
4. K. Sieh *et al.*, *Science* **260**, 171 (1993).
5. In general, seismic energy is scattered by lateral variations in velocity and density over length scales comparable to, or shorter than, seismic wavelength. To quantify scattering, I use a significance scale (scattering potential), rather than absolute strength of scattering, because of the difficulty of accurately modeling amplitudes of high-frequency crustal waves. Tests performed with synthetic data sets demonstrate a monotonic, but nonlinear, mapping of scattering strength to significance.
6. This pattern is partly a result of the limited ray-parameter coverage afforded by teleseismic events, which, coupled with frequency band constraints (~0.1 to 1 Hz), renders KCM unable to image the narrow (10 to 200 m), near-vertical, low-velocity fault zones that often characterize the structural expression of faulting at shallow depths (<5 to 10 km) [W. D. Mooney and A. Ginzburg, *Pure Appl. Geophys.* **124**, 141 (1986); Y.-G. Li, K. Aki, D. Adams, A. Hasemi, W. H. K. Lee, *J. Geophys. Res.* **99**, 11705 (1994)].
7. Length scale is quoted as semivariogram offset at 80% of variance. Active fault density is defined as total mapped fault length resolved on the scattering grid (0.01° by 0.01°). Seismic measures of the length scale of heterogeneity, based on *P*-wave coda duration and amplitude, yield comparable estimates [C. A. Powell and A. S. Meltzer, *Geophys. Res. Lett.* **11**, 481 (1984); A. Frankel and R. W. Clayton, *J. Geophys. Res.* **91**, 6465 (1986); see also (*2*)].
8. The nominal significance of this correlation exceeds 99.99% on the assumption that all samples are independent. The assumption of an 8-km correlation length scale (*7*) results in a conservative estimate of 99.5% significance.
9. R. Wu and K. Aki, *Geophysics* **50**, 582 (1985).
10. Scattering vanishes along strike and normal to a single crack [W. M. Visscher, *J. Acoust. Soc. Am.* **69**, 50 (1981)]. Scattering from a cracked volume is complex and need not vanish entirely [R. L. Gibson and A. Ben-Menahem, *J. Geophys. Res.* **96**, 19905 (1991)].
11. Angles are expressed as the minimum of trend to strike and trend to fault normal; the maximum is 45°.
12. E. Hauksson, L. M. Jones, K. Hutton, D. Eberhart-Phillips, *J. Geophys. Res.* **98**, 19835 (1993).
13. R. C. Aster and P. M. Shearer, *Geophys. J. Int.* **108**, 740 (1992); H. Kern and H.-R. Wenk, *J. Geophys. Res.* **95**, 11213 (1990).
14. T. Jones and A. Nur, *Geology* **10**, 260 (1982).
15. S. Crampin, R. Evans, B. K. Atkinson, *Geophys. J. R. Astron. Soc.* **76**, 147 (1984).
16. E. Hauksson, *Bull. Seismol. Soc. Am.* **84**, 917 (1994).
17. S. Kaneshima, *J. Geophys. Res.* **95**, 11121 (1990).
18. P. C. Leary, Y.-G. Li, K. Aki, *Geophys. J. R. Astron. Soc.* **91**, 461 (1987); Z. Zhang and S. Y. Schwartz, *J. Geophys. Res.* **99**, 9651 (1994).
19. T. Lay and H. Kanamori, in *Earthquake Prediction, An International Review*, D. Simpson and P. Richards, Eds. (Maurice Ewing Series 4, American Geophysical Union, Washington, DC, 1981), pp. 579–592.
20. A. Jin and K. Aki, *J. Geophys. Res.* **94**, 14041 (1989).
21. B. P. Cohee and G. C. Beroza, *Bull. Seismol. Soc. Am.* **84**, 692 (1994).
22. Cross-fault scattering variance is measured as the variance of scattering within 20-km-wide by 2-km-long bins along the fault.
23. T. K. Rockwell *et al.*, *Eos* **74**, 67 (1993).
24. T. J. Sheppard, *J. Geophys. Res.* **95**, 11115 (1990).
25. Y.-G. Li, T.-L. Teng, T. L. Henyey, *Bull. Seismol. Soc. Am.* **84**, 307 (1994).
26. C. H. Scholz, *The Mechanics of Earthquakes and Faulting* (Cambridge Univ. Press, Cambridge, 1990).

27. Supported by NSF award EAR-9417493. Institute of Tectonics contribution 282.

20 June 1995; accepted 25 September 1995

North Atlantic Deepwater Temperature Change During Late Pliocene and Late Quaternary Climatic Cycles

Gary S. Dwyer,* Thomas M. Cronin, Paul A. Baker, Maureen E. Raymo, Jeffrey S. Buzas, Thierry Corrège†

Variations in the ratio of magnesium to calcium (Mg/Ca) in fossil ostracodes from Deep Sea Drilling Project Site 607 in the deep North Atlantic show that the change in bottom water temperature during late Pliocene 41,000-year obliquity cycles averaged 1.5°C between 3.2 and 2.8 million years ago (Ma) and increased to 2.3°C between 2.8 and 2.3 Ma, coincidentally with the intensification of Northern Hemisphere glaciation. During the last two 100,000-year glacial-to-interglacial climatic cycles of the Quaternary, bottom water temperatures changed by 4.5°C. These results show that glacial deepwater cooling has intensified since 3.2 Ma, most likely as the result of progressively diminished deepwater production in the North Atlantic and of the greater influence of Antarctic bottom water in the North Atlantic during glacial periods. The ostracode Mg/Ca data also allow the direct determination of the temperature component of the benthic foraminiferal oxygen isotope record from Site 607, as well as derivation of a hypothetical sea-level curve for the late Pliocene and late Quaternary. The effects of dissolution on the Mg/Ca ratios of ostracode shells appear to have been minimal.

Deep-ocean circulation affects the storage and transfer of heat and nutrients in the ocean, as well as atmospheric CO_2 (*1–3*). Attempts to evaluate deep-ocean bottom water temperature (BWT) changes, which accompany climate-driven changes in deep-ocean circulation, have focused on the benthic foraminiferal oxygen isotope ($\delta^{18}O$) record, but results have been equivocal. Emiliani (*4*) first postulated that glacial-to-interglacial variations in the $\delta^{18}O$ in benthic foraminifers reflected changes in both ice volume and BWT. Later, Shackleton (*5*) ascribed the $\delta^{18}O$ variations mainly to changes in ice volume. Recognition of the differences in the $\delta^{18}O$ records of various deep-sea cores and the discordance between sea-level records (*6*) and the $\delta^{18}O$ record, however, led Chappell and Shackleton (*7*) to propose that deep Pacific glacial BWTs were 1° to 1.5°C, and possibly 2.5°C, lower than interglacial tem-

G. S. Dwyer and P. A. Baker, Department of Geology, Duke University, Durham, NC 27708, USA.
T. M. Cronin, U.S. Geological Survey, Branch of Paleontology and Stratigraphy, Mail Stop 970 National Center, Reston, VA 22092, USA.
M. E. Raymo, Department of Earth, Atmospheric, and Planetary Sciences, Massachusetts Institute of Technology, Cambridge, MA 02139, USA.
J. S. Buzas, Department of Mathematics and Statistics, University of Vermont, Burlington, VT 05051, USA.
T. Corrège, Département de Géologie et Océanographie, Université de Bordeaux I, Avenue des Facultés, Bordeaux, France.

*To whom correspondence should be addressed.
†Present address: Laboratoire des Formations Superficielles, ORSTOM, 32 Avenue Henri Varagnat, 93143 Bondy Cedex, France.